www.ietdl.org

Published in IET Image Processing
Received on 5th February 2014
Revised on 15th July 2014
Accepted on 31st July 2014
doi: 10.1049/iet-ipr.2014.0106

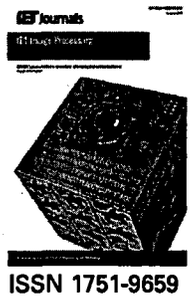

ISSN 1751-9659

Active contours with prior corner detection to extract discontinuous boundaries of anatomical structures in X-ray images

Aruni U.A. Niroshika[1], Ravinda G.N. Meegama[2], Ravindra S. Lokupitiya[3], Donna K.S. Kannangara[4]

[1]Department of Information Technology, Faculty of Computing, Sri Lanka Institute of Information Technology, Malabe, Sri Lanka
[2]Department of Computer Science, Faculty of Applied Sciences, University of Sri Jayewardenepura, Nugegoda, Sri Lanka
[3]Department of Statistics, Faculty of Applied Sciences, University of Sri Jayewardenepura, Nugegoda, Sri Lanka
[4]Oral and Maxillofacial Unit, General Hospital, Kalutara, Sri Lanka
E-mail: rgn@sci.sjp.ac.lk

Abstract: Active contours are a form of curves that deforms according to an energy minimising function and are widely used in computer vision and image processing applications to extract features of interests from raw images acquired using an image capturing device. One of the major limitations in active contours is its inability to converge accurately when the object of interest exhibits sharp corners. In this study, a new technique of active contour model to extract boundaries of objects having sharp corners is presented. By incorporating a priori knowledge of significant corners of the object into the deforming contour, the proposed active contour is able to deform towards the boundaries of the object without surpassing the corners. The ability of the new technique to accurately extract features of interest of anatomical structures in medical X-ray images having sharp corners is demonstrated.

1 Introduction

Image segmentation and boundary detection are the challenging tasks in the area of image processing and the techniques developed to achieve these tasks facilitate many computer vision based applications. Numerous techniques and models have been developed to accomplish this segmentation task, specific for different contexts. In the context of medical image analysis, deformable active contour models are the widely accepted models, which are used to segment medical images such as computer tomography, magnetic resonance imaging, X-ray and ultrasound images [1, 2].

A noteworthy challenge in the arena of medical imaging is segmenting boundaries of same structure of interest [3]. Although various medical image segmentation techniques have been developed to achieve this task, they do not produce accurate results because of anomalies present in medical images such as high noise level, image blur, low contrast, irregular boundaries and several unwanted structures that surround the object under observation.

Deformable models are used to segment medical images by incorporating a priori knowledge of the structure such as the position, area and the shape that can be blended with image data itself. These models can be further classified into two categories, namely, parametric and geometric models. In parametric models, the initial contour is defined as a set of parametric curve segments which get attracted towards the targeted object by varying its shape over space and time. Parametric models are ideal in many image processing scenarios such as to extract very thin structures, when the structures consist of highly irregular boundaries, and in real-time segmentation [4].

There are two types of formulations for parametric deformable models: energy minimising and dynamic force formulation. The energy minimising formulation behaves according to the minimum principle while the dynamic force formulation depends on external forces. The original snake [5] has several limitations on its performance. Thus, several new ideas, such as topological adaptive [6, 7], balloon [8], fast greedy [9], gradient vector flow (GVF) [10], geodesic [11], B-spline [12] and non-uniform rational B-splines (NURBS) [13], have been proposed. Although deformable models are still claimed to be the most successful model-based approaches to segment medical images [14], associated problems such as poor capture range, initialisation errors, problems with the concavities, high user interaction and problems with sharp corners have not been addressed fully in the literature.

The former snake models given above [5–13] are unable to capture sharp discontinuous corners of the target object precisely. This paper proposes a new technique to overcome the above problems. First, significant corners of the desired object are selected manually by the operator or automatically by a corner detection algorithm such as the

Harris corner detector [15]. By re-parameterising the model at user-specified iterations of the deformation process, the pre-defined corner points are added to the deforming snake. Experiments indicate that the new technique can improve the snake's precision to capture the boundary with sharp corners, a task that is difficult to accomplish with former models.

2 Parametric deformable model

The snake s is defined as a parametric curve $v(s) = (x(s), y(s))^T$, where x and y are the coordinates of a given snaxel. The total energy of the snake, E_{snake}, is defined as

$$\begin{aligned} E_{\text{snake}} &= \int_0^1 E_{\text{snake}}(v(s))\mathrm{d}s \\ &= \int_0^1 E_{\text{internal}}(v(s)) + E_{\text{image}}(v(s)) + E_{\text{con}}(v(s))\mathrm{d}s \end{aligned} \tag{1}$$

where E_{internal} represents the internal energy because of stretching and bending, E_{image} refers to image energy derived from image data and E_{con} is the constraint energy. The summation of the image energy E_{image} and the constraint energy E_{con} is known as the external energy.

The internal energy of the snake is given as

$$E_{\text{internal}} = (\alpha(s)|v_s(s)|^2 + \beta(s)|v_{ss}(s)|^2)/2 \tag{2}$$

where $|v_s(s)|^2$ determines the elasticity and $|v_{ss}(s)|^2$ gives the curvature of the parametric curve which forms the deforming snake. The parameters $\alpha(s)$ controls the 'tension' while $\beta(s)$ controls the 'rigidity'.

The image energy E_{image}, is written as

$$E_{\text{image}} = -|\nabla I(x, y)|^2 \tag{3}$$

where $\nabla I(x, y)$ is the gradient of the image I at (x, y).

A snake that minimises the total energy must satisfy the Euler equation

$$\alpha x''(s) - \beta x''''(s) - \nabla E_{\text{image}} = 0 \tag{4}$$

To express the physical motion of the snake, the expression can be further written as a force balanced equation as:

$$F_{\text{internal}} + F_{\text{external}} = 0 \tag{5}$$

where $F_{\text{internal}} = \alpha x''(s) - \beta x''''(s)$ and $F_{\text{external}} = -\nabla E_{\text{image}}$

The snake deforms over time towards the desired object minimising the total energy E_{snake}. If $v(s, t)$ denotes a point on a dynamic curve at time t, the point at time $t+1$, $v(s, t+1)$ is given as

$$v(s, t+1) = \arg \min_{v(s,t) \in V} E_{\text{snake}} v(s, t) \tag{6}$$

where v is the set of all potential curve points $v(s, t)$.

3 Recent work

The original snake model [5] must be initialised closer to the desired object to obtain accurate results. As an example, if the initial contour is plotted far away from the object boundary, the snake tends to move arbitrarily because of the absence of an image force or it might deform towards incorrect lines, edges and noise points.

The T-snake [7] exhibits more robustness over the former method because of its topological flexibility. Snakes with balloon forces have been introduced recently having the capability to determine the direction automatically by analysing the region information of the image [8, 16, 17]. However, these balloon models are incapable of capturing irregular boundaries, sharp corners, weak edges and sometimes forms circular loops. Another landmark is introduced by adding a distance potential force into the snake [18] that exploits the concept of a distance map in which it keeps the track of the distance between each pixel and its nearest boundary point [19]. Unfortunately, this model too is unable to deform accurately into boundaries with concavities and sharp corners.

Xu and Prince [10, 20] have proposed a new deformable model called GVF snake where the spatial distribution of the gradient is considered to calculate the quality of the edge. This model is also capable of deforming towards the remote object regardless of its initial position. Caselles [11] and Malladi [21] have introduced the geodesic active contour model based on the evolution theory [22, 23] and the level set method [24].

All the above snake models suffer from a common drawback, known as global propagation, in that even a slight movement on an individual snaxel will globally propagate through the entire snake so that the movement of each snaxel cannot be treated separately. As a solution, Menet [12] introduced the B-spline snake supporting local control [25, 26]. Unfortunately, this model handles local control by adding extra control points during deformation. Based on this phenomena, dynamic-NURBS (D-NURBS) [27] and NURBS [13] snake models, having local control, are introduced. Although a NURBS snake has the ability to deform without adding more control points near high curvature regions, it is unable extract a discontinuous boundary as NURBS are inherently continuous.

As such, none of the above implementations provide a satisfactory solution for extracting complex object boundaries with sharp (discontinuous) corners.

4 Methodology

4.1 Sharp corners

The issue of the snake surpassing corner points and sliding into the object occur because of the strength of the elasticity force as well. The elasticity force is responsible for holding the curve together (by minimising the distance between two adjacent snaxels at each deformation step) while shrinking towards the targeted object. However, if the distance between two adjacent snaxel points is too high, especially near a corner, the elasticity force tries to drag the snaxel away from the corner and into the object as shown in Fig. 1*a*.

4.2 Definition of corner points and initialisation

Perhaps the most widely used corner detector is the Harris operator [15] which is based on the local auto-correlation function of a signal. Given a shift $(\Delta x, \Delta y)$ and a point

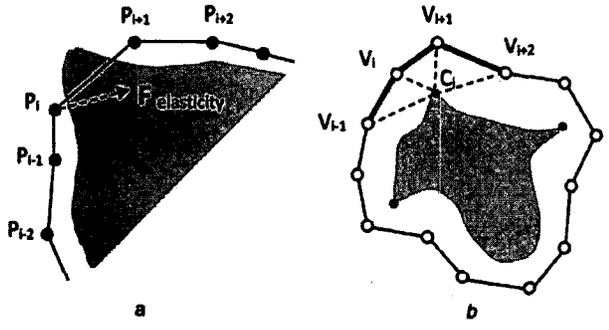

Fig. 1 *Behaviour of snakes near sharp corners*

a Elasticity force $F_{elasticity}$ drags the snaxel into the object near the sharp corner

b Position of the initial contour located around the target object (shaded region)

(x, y), the auto-correlation function is defined as

$$C(x, y) = \sum_{w} [I(x_i, y_i) - I(x_i + \Delta x, y_i + \Delta y)]^2 \quad (7)$$

At the initial step, all the significant corners of the desired object are detected either using Harris operator or by manual placement. The corner points, numbering n, are placed in a separate array as

$$\text{corner\_points}[] = \{C_i(x, y) | i = 0, 1, 2, \ldots, n-1\} \quad (8)$$

The initial contour is plotted 15–25 pixels outside (this range is empirically selected) the desired object boundary using a set of snaxel, numbering m, kept at equal distances apart. These snaxels are placed in a separate array as

$$\text{snaxel\_points}[] = \{V_i(x, y) | i = 0, 1, 2, \ldots, m-1\} \quad (9)$$

The algorithm finds the nearest four adjacent snaxels to each C_i by considering the distance between the corner point and each snaxel to extract the nearest three adjacent curve segments to each corner point. As illustrated in Fig. 1*b*, $V_{i-1} - V_i$, $V_i - V_{i+1}$ and $V_{i+1} - V_{i+2}$ are the nearest three adjacent curve segments to the user defined C_i. Therefore it reduces the amount of computation required to find the nearest curve segment at each re-parameterisation step. These three nearest curve segments, associated with each corner point, are stored and tracked along with the corner point and are recalculated and modified after each re-parameterisation step. The model then starts deflating towards the object boundary by minimising E_{snake}.

4.3 Deformation and re-parameterisation

The proposed model is re-parameterised after every r time steps, referred to as a deformation step which is set empirically between 5 and 10 by the user. The threshold T_d gives the distance between a specific corner point and its nearest curve segment and is again set empirically between 4 and 7. If the boundary of the target object does not contain a corner region, T_d is placed on a higher value. On the other hand, if the boundary of a specific object contains corners or concavities, T_d must be undoubtedly low. Apart from that, low values for T_d helps the snake to preserve the smoothness and the shape during deformations. However, it is advisable to maintain a low value for r if T_d is low.

After each deformation step r, a local search computes the absolute perpendicular distance d from each corner point to its nearest candidate contour segments. If $d < T_d$, C_i is added between the respective curve segments and it is declared as a new snaxel. Subsequently, this particular curve segment is pushed/pulled towards the corner point. If there are several distances that fall less than the T_d, the algorithm selects the closest curve segment. Now, the corner point is merged with the deforming snake and becomes a new snaxel of the updated snake.

The movement of the newly added corner point is restricted to remain stable during the deformation. At the same time, the second-order continuity term is released (set $\beta = 0$) on C_i to facilitate building up the contour near the corner. However, the rest of the snaxels can move the contour towards the target object by minimising the total energy of the snake.

After adding a new corner point, the new set of curve segments should be detected again from the beginning for the remaining corner points. This new corner point is removed from 'corner_points' [] and added into the correct position in 'snaxel_points' []. As an example; after five iterations ($r = 5$), if $d < T_d$, C_i is added in between V_i and V_{i+1} as shown in Fig. 2*a* and C_i is also considered as a snaxel of the deforming contour. The parameter T_d controls the deformation speed of the curve segment towards the nearest corner point. For example, if $T_d = 5$ and when the curve segment $V_i - V_{i+1}$ is closer ($d < 5$) to C_i, the curve segment $V_i - V_{i+1}$ steps over more than one pixel but less than four pixels towards the corner point.

However, in certain cases, the contour may step over the corner point as well. Note that in Fig. 2*c*, the curve segment $V_{i+1} - V_{i+2}$ has already stepped over C_j. In such a scenario, the curve segment is pulled backwards to the corner area during the next re-parameterisation step.

Figs. 2*b* and *d* also depicts the new connection after adding $C_i$and C_j into the deforming snake. The arrows represent the

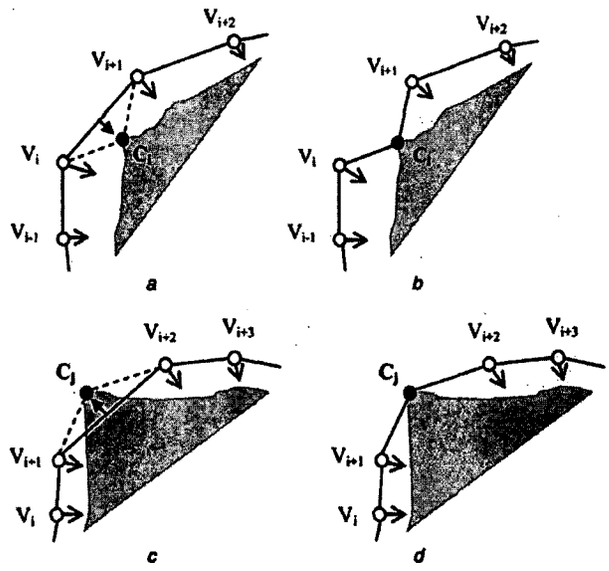

Fig. 2 *Re-parameterisation step of the deforming snake*

a $d < T_d$

b Corner point C_i is added between V_i and V_{i+1} and the curve segment is pushed towards the corner

c $d < T_d$

d Corner point C_j is added between V_{i+1} V_{i+2} the curve segment is pulled back to the corner

doi: 10.1049/iet-ipr.2014.0106

ALGORITHM

// Specify $\alpha, \beta, \gamma, T_d, d, r, N$ = number of iterations
// n = total number of corner points detected by the Harris operator
// m = total number of snaxels defined by the operator

Step 1:
corner_points [ ] = getCornerPoints (Harris corner detector / mouse input)
snaxel_points [ ] = getCotrolPoints (mouse input)

//Finding the nearest three adjacent curve segments
Step 2: For each corner point C_i:
2.1: Calculate the distance d from C_i to each snaxel
2.2: Select four nearest adjacent control points
2.3: Select three nearest adjacent curve segments

Step 3: Deform the initial contour according to energy minimising formulation
3.1: After each deformation step r, for each corner point:
3.1.1: Compute d from the corner point to each contour segment
If $d < T_d$;

- Push/Pull the curve segment towards C_i
- Add C_i into the corresponding contour segment
- Release β on r point C_i and restrict the movement
- Remove C_i from *corner_points*[ ]
- Push C_i into *snaxel_points*[ ]
- Go back to Step 2

Fig. 3 *Initialisation, deformation and re-parameterisation*

direction of movement of the curve segment towards the object boundary.

The algorithm given below explains the deformation scheme of the proposed model (See Fig. 3).

5 Results and discussion

The proposed model is tested on synthetic images of simple two-dimensional shapes to X-ray images of human anatomical structures. For all the experiments, the model parameters used are: $r = 5$, $T_d = 5$, $\alpha = 0.40$, $\beta = 0.20$ and $\gamma = 1.00$ and the stopping criterion = 200 iterations. Although these parameters are selected empirically, the corner points are manually marked exactly on top of the significant corners. The performance of the proposed snake model is compared with the major landmark snake models, namely, Kass [5], balloon [8], GVF [10] and NURBS [13].

The average distance error (e) [28] is used to validate the accuracy of the test results as follows

$$e(v, \hat{v}) = \frac{1}{L}\int_S \min_{s' \in \hat{v}} |v(s) - \hat{v}(s)| ds \tag{10}$$

where $v(s)$ represents the original contour position of the deformed snake, $\hat{v}(s)$ represents the extracted true boundary of the target object and L is the length of the snake. For all the experiments, the actual boundary around the target

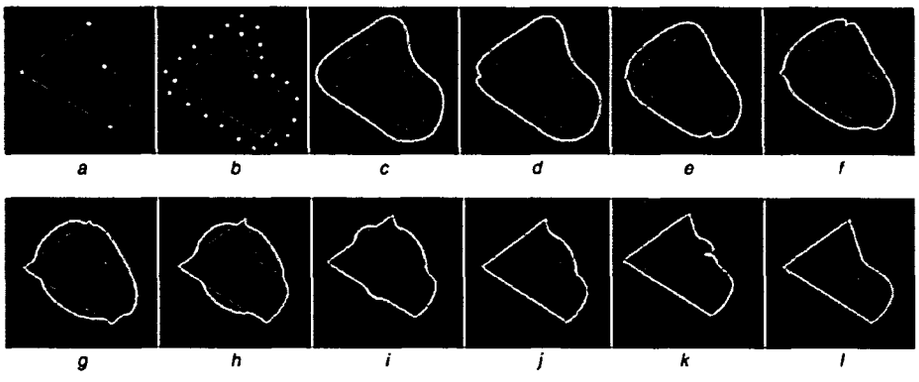

Fig. 4 *Deformation of the proposed snake model in a synthetic image*

a Corner points defined by the operator
b Initial contour
c to *k* Intermediates taken after each 30 iterations
l Final position after 300 iterations

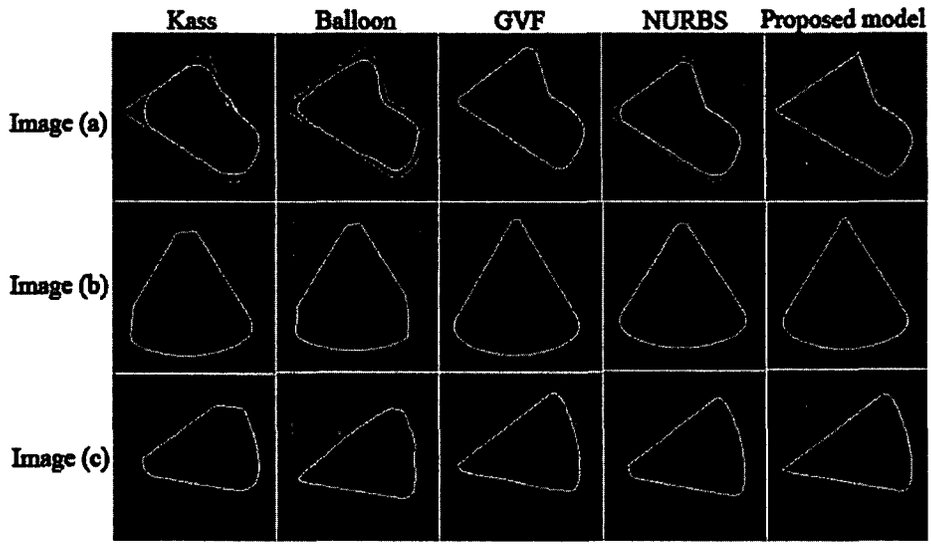

Fig. 5 *Convergence of the five different snake models on three different synthetic images: (first column) Kass snake, (second column) balloon snake, (third column) GVF snake, (fourth column) NURBS snake and (fifth column) proposed snake*

Table 1 Comparison of average distance errors (e) for different snake models applied to images in Fig. 5

Image	Average distance error (*e*)				
	Kass	Balloon	GVF	NURBS	Proposed
Fig. 5*a*	6.73	5.78	2.76	3.21	0.87
Fig. 5*b*	5.35	6.10	1.23	1.32	0.08
Fig. 5c	5.90	5.68	1.31	2.34	0.03

Table 2 Comparison of average distance errors (*e*) for different snake models applied on the synthetic image in Fig. 4

Snake model				
Kass	balloon	GVF	NURBS	proposed
8.81	6.92	5.72	6.82	1.59

object is manually obtained by carefully sketching it out by a skilled medical clinician.

5.1 Experiments with synthetic images

The convergence ability of the proposed algorithm is tested on a synthetic image of size 256 × 256 pixels where the region of interest (ROI) contains three sharp corners as in Fig. 4. Four corner points are manually marked exactly on top of the corner regions of the object by the operator and the initial contour is plotted using 21 snaxels.

In this experiment, after every fifth iteration, the deforming snake performs a local search for significant corners within a radius of 5 pixels ($r = 5$ and $T_d = 5$). If a corner is present, it is added and the snake is re-parameterised. This behaviour is clearly seen in Fig. 4*d* where the contour is attracted towards the left significant corner during deformation. Capturing the remaining two corner points are shown in Figs. 4*e* and *f*. It can also be noted in Figs. 4*g* –*i* that the snake is still moving towards the target object while restricting further movement near the corners already detected.

Table 3 Average distance errors (e) obtained by the proposed snake model under different SNR values on the synthetic image in Fig. 4

	SNR					
	5	10	15	20	25	30
average distance error (*e*)	2.91	2.69	1.59	0.87	0.24	0.08

Furthermore, the performance of the proposed algorithm is compared with respect to existing major snake models as in Fig. 5. Three synthetic images of size 256 × 256 pixels are selected where the ROI contains discontinuous corners. The same initial contour and model parameters are used to initialise the same object using all five different snake models. Table 1 gives the accuracy of boundary extraction of the above experiment using the average distance errors [28]. It is notable that the error values are considerably low in the proposed model.

The X-ray images inherently contain a considerable amount of noise. Therefore the robustness of the proposed snake is further tested in the presence of noise by adding Gaussian noise into the synthetic image in Fig. 4 to form a signal-to-noise ratio (SNR) of 15. Table 2 shows the corresponding standard distance errors of this experiment.

As seen in Table 2, the performance of the proposed model is best when compared to others. The model is also further tested with different noise levels where the SNR varies from 5 to 30 on the same synthetic image. The resulting average distance errors are given in Table 3 which indicates that the proposed snake model performs well for the images having an SNR of >20.

5.2 Experiments with real medical images

The edges in medical images are extremely difficult to extract using non-adaptive segmentation algorithms because of high noise levels, low contrast, discontinuous boundaries, etc. The capability of the proposed model to detect discontinuous boundaries is tested using several X-ray images of human bones with a fracture. Such images are useful to test the

doi: 10.1049/iet-ipr.2014.0106

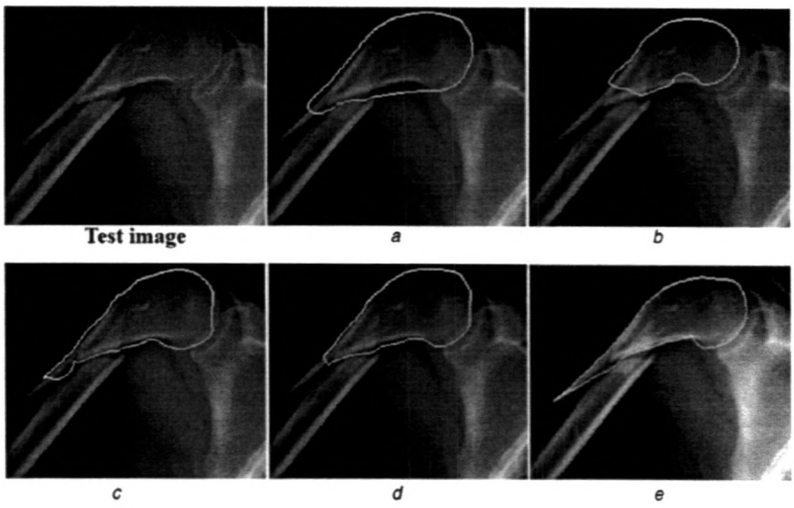

Fig. 6 *Illustrations of convergence of a linear fracture of the arm bone with*

a Kass snake
b Balloon snake
c GVF snake
d NURBS snake
e Proposed snake model

proposed algorithm because these objects contain very-sharp regions near the fractured spot. First, an X-ray image of size 256 × 256 pixels is selected where the ROI is an arm bone having a very-sharp linear fracture as seen in Fig. 6.

Five different snake models are used to extract the head side of the fractured arm bone as seen in Fig. 6. In all cases, a skilled clinician placed the initial contour and a single corner point at the sharp tip (right side) of the fractured bone. Table 4 shows the corresponding standard distance errors (*e*) of this experiment.

The proposed model is also tested with four different X-ray images of human bones injured by a fracture. These images are arbitrarily selected from a 25 image data set obtained from (http://www.shutterstock.com/). Fig. 7 illustrates the convergence results of the proposed model on each image and Table 5 gives the corresponding average distance errors (*e*). As seen, the proposed model managed to extract the boundary of the desired object while capturing the sharp regions with an increased accuracy than other models.

Detecting the accurate physical shape of a bone fracture is useful when it is difficult to measure and quantify the extent of injury by performing an external examination. The accurate physical shape of the fractured region facilitates an orthopaedic surgeon to decide on subsequent treatment protocols.

The proposed snake model is further tested on a dental X-ray image (http://periodontics-dentalimplants.com) as seen in Fig. 8 to detect the exact boundary and the shape of each tooth. The initial contour is first plotted by a skilled clinician using 20 snaxel points for all the cases and additional corner points are defined near the sharp corners of the ROI.

Table 4 Comparison of average distance errors (*e*) for different snake models applied on the image in Fig. 6 (bone fracture of the arm)

Snake model				
Kass	balloon	GVF	NURBS	proposed
7.34	9.09	5.72	6.81	1.21

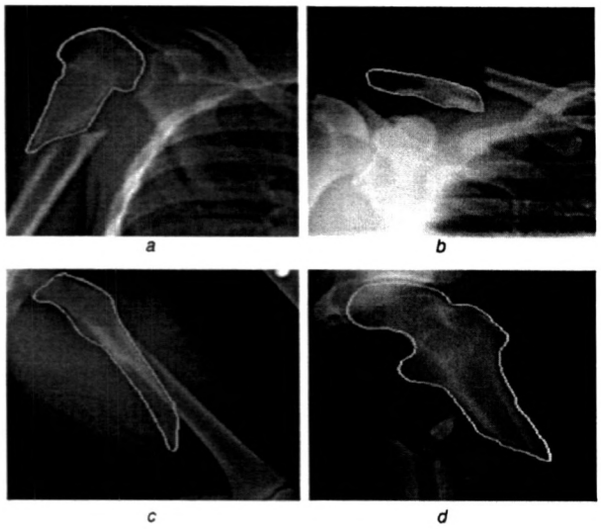

Fig. 7 *Convergence of the proposed snake*

a Pathological fracture on right humerus because of bone cyst
b Broken collar bone
c Linear fracture
d Fractures of the greater trochanter

Table 5 Average distance errors (e)) for different snake models applied to images in Fig. 7

Snake model	Average distance error (e)			
	Fig. 7*a*	Fig. 7*b*	Fig. 7*c*	Fig. 7*d*
Kass	6.35	4.24	4.98	5.92
balloon	5.24	5.49	4.51	5.01
GVF	3.02	2.94	3.24	4.92
NURBD	4.09	1.38	3.95	3.93
proposed	1.21	0.82	0.92	1.21

The top image in Fig. 8 represents the maxillary (upper jaw) and mandibular (lower jaw) teeth of an adult. The proposed model is applied on each tooth showing

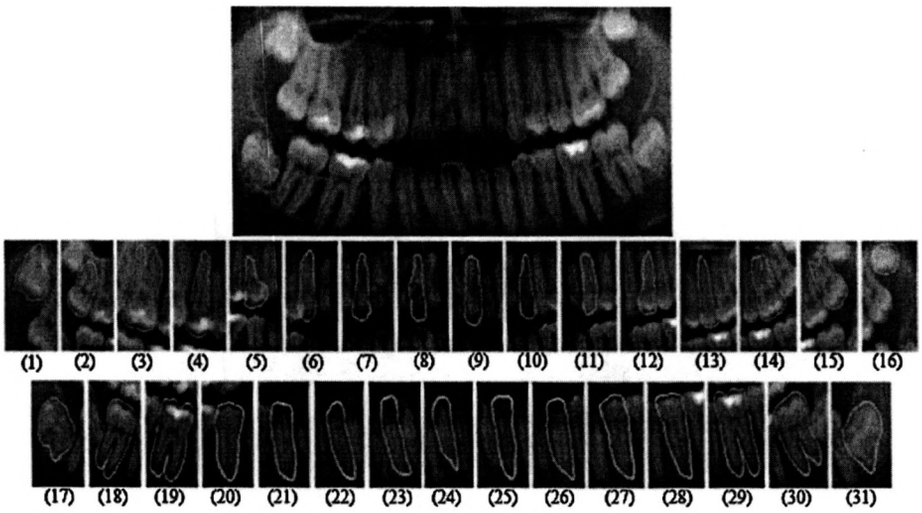

Fig. 8 *Extraction of boundaries of teeth from dental X-ray images*
(top) dental X-ray image of teeth and (bottom two rows) convergence of the proposed snake on each tooth

discontinuities and sharp regions. The same initial contour and model parameters are used to initialise the same tooth using all five different snake models. Each model is applied on 31 different teeth separately and the average distance errors (e) are given in Table 6.

In order to confirm the test results statistically, we first conducted one-way analysis of variance (one-way analysis of variance (ANOVA) for five different groups with a 5% significance level. The ANOVA output values ($F = 124.09$ and $P\text{-}value = 0.000$ with $R^2 = 76.79$) revealed that there is a significant difference between mean distance error values of the groups.

Because of the significant difference of average distance errors between the groups, Tukey's pairwise comparisons are performed by taking two groups at a time (proposed model with one of the other models). As seen in Table 7, a significant difference of distance errors between the proposed model and each one of the other models are observed.

Consequently, as seen in Table 8, it is evident that the mean value of the proposed model is comparatively low (1.78), meaning a good segmentation. Such accurate detection of the shape of each tooth is important during teeth replacements, tracking substantial changes in the shapes and

Table 6 Average distance errors (e) for different snake models applied to images in Fig. 8

Image	Average distance errors (e)				
	Kass	Ballon	GVF	NURBS	Proposed
Fig. 8(1): maxillary right third molar	6.33	5.33	3.23	2.90	1.03
Fig. 8(2): maxillary right 2nd molar	6.25	5.23	1.94	2.88	1.19
Fig. 8(3): maxillary right 1st molar	5.94	4.35	2.00	3.02	1.23
Fig. 8(4): maxillary right second premolar (bicuspid)	6.09	4.14	2.82	3.28	1.22
Fig. 8(5): maxillary right first premolar (bicuspid)	6.12	5.09	3.93	2.99	1.71
Fig. 8(6): maxillary right canine	5.92	5.94	3.02	3.01	1.23
Fig. 8(7): maxillary right lateral incisor	5.99	6.92	2.03	2.98	1.44
Fig. 8(8): maxillary right central incisor	7.94	6.74	3.41	4.09	3.22
Fig. 8(9): maxillary left central incisor	6.42	4.34	3.00	3.91	1.50
Fig. 8(10): maxillary left lateral incisor	7.01	5.23	4.02	3.65	2.01
Fig. 8(11): maxillary left canine	7.42	5.93	4.25	3.90	2.13
Fig. 8(12): maxillary left first premolar	6.91	5.00	3.33	2.97	1.89
Fig. 8(13): maxillary left second premolar	5.94	5.02	4.35	2.83	1.01
Fig. 8(14): maxillary left first molar	4.51	4.24	3.33	2.12	1.24
Fig. 8(15): maxillary left second molar	5.15	4.23	4.91	3.82	1.83
Fig. 8(16): maxillary left third molar	5.55	5.33	4.10	3.09	1.34
Fig. 8(17): mandibular right third molar	6.01	5.70	5.35	4.02	2.09
Fig. 8(18): mandibular right second molar	6.32	6.09	5.41	2.34	2.13
Fig. 8(19): mandibular right first premolar	7.32	6.35	5.92	5.02	4.98
Fig. 8(20): mandibular right first premolar	6.23	4.35	4.24	2.35	1.25
Fig. 8(21): mandibular right canine	5.35	4.00	2.92	3.34	0.98
Fig. 8(22): mandibular right lateral incisor	5.42	5.94	2.42	2.32	1.09
Fig. 8(23): mandibular right central incisor	5.25	4.25	3.29	3.19	1.24
Fig. 8(24): mandibular left central incisor	5.67	4.24	2.40	2.08	1.23
Fig. 8(25): mandibular left lateral incisor	6.26	5.28	3.49	2.82	2.45
Fig. 8(26): mandibular left canine	6.14	6.41	4.24	2.34	2.65
Fig. 8(27): mandibular left first premolar	5.33	4.04	3.99	2.08	1.10
Fig. 8(28): mandibular left second premolar	5.14	4.02	3.43	3.24	1.08
Fig. 8(29): mandibular left first molar	7.42	5.92	4.92	4.24	3.52
Fig. 8(30): mandibular left second molar	6.97	5.59	3.46	3.92	2.12
Fig. 8(31): mandibular left third molar	6.78	5.32	4.25	3.33	2.12

doi: 10.1049/iet-ipr.2014.0106

Table 7 Tukey's simultaneous tests applied on different snake models

	Tukey's pairwise comparisons					
	T	*P*-value	Mean difference	Std. error difference	95% confidence interval of the difference	
					Lower	Upper
proposed against Kass	20.10	0.00	4.38	0.218	3.78	4.99
proposed against balloon	15.57	0.00	3.40	0.218	2.79	4.00
proposed against GVF	8.60	0.00	1.88	0.218	1.27	2.48
proposed against NURBS	6.33	0.00	1.38	0.218	0.78	1.98

Table 8 Comparison of mean values of average distance errors (e) between the snake models

	N	Mean	Std. deviation	Std. error	95% Confidence interval for mean		Minimum	Maximum
					Lower bound	Upper bound		
Kass	31	6.17	0.79	0.14	5.88	6.45	4.51	7.94
balloon	31	3.66	1.01	0.18	3.29	4.03	1.94	5.92
GVF	31	3.66	1.01	0.18	3.29	4.03	1.94	5.92
NURBS	31	3.16	0.71	0.13	2.90	3.43	2.08	5.02
proposed	31	1.78	0.88	0.16	1.46	2.11	0.98	4.98

the position of the teeth after certain treatments and automating the process of forensic dentistry to recognise individuals when other cues of biometric identification (e.g. fingerprint, blood samples, face and so on) are not available.

The balloon snake gives a slightly better result in capturing corner regions compared to the original Kass model. The coefficients of elasticity and curvature have a great effect on the behaviour of the evolving snake in that if α and β are high, the internal energy has a major influence over image forces resulting in the curve becoming smooth. The GVF gives poor results near sharp corners as it has a tendency to produce a continuous curve near a sharp region of the desired object.

The proposed model is useful in medical imaging to segment fractured bones, tiny tissues, discontinuous anatomical structures, teeth and so on where detecting discontinues boundaries helps medical practitioners to arrive at important conclusions to provide better treatment options. The main reason for the proposed model to demonstrate better results on detecting corners compared with the other existing models is the inclusion of a priori knowledge about the significant corner points at the boundary of the target object into the deformation process. At certain times, however, the contour may step over the corner point after a certain number of iterations. This situation may occur if T_d is quite high. Even in such a scenario, during the next re-parameterisation step, it has the ability to pull the curve back to reach a corner point and recapture the actual boundary.

The accuracy of the proposed model is based on the values of its model parameters. Tuning of contour parameters α, β, γ, r and T_d is an image specific process and has to be performed empirically for each of the analysed image types. A distance of 20 pixels between adjacent snaxels is maintained to facilitate computation of the perpendicular distance to the nearest curve segment.

With respect to computational complexity, the original Kass model needs to perform matrix-vector multiplications over the penta-diagonal banded matrix taking $O\ (n^2)$ iterations to traverse through the entire length of the snake to solve the fully explicit Euler equations. Although the balloon snake consumes the same time complexity as that of the original Kaas model, the GVF snake has a relatively high computational complexity of $O\ (n^2m^2)$. The computational complexity of the NURBS snake, which is a spline-based formulation, is $O\ (k^2n)$, where n is the number of control points over the snake and k is the degree of the spline. In the proposed snake model, the re-parameterisation step consumes the longest time taking $O\ (nm)$, where n is the number of re-parameterisation steps and m is the number of corner points.

The proposed snake model suffers from few limitations as well. The detection of the closest curve segment from each corner point after each deformation step is a computationally intensive process. Unfortunately, this cannot be avoided as the local search and computational steps should be carried out continuously while the contour deforms. Secondly, the application of the Harris operator to detect corner points is limited and it purely depends on the nature of the image under consideration. If a point having strong intensity exists between the region of the target object boundary and the initial contour, the Harris operator tends to detect such a point also as corner yielding a false segmentation. In such a case, where the intensity variation within this region is not uniform, the operator must manually define the corner points. We have integrated such manual operations to the proposed snake model to overcome such anomalies.

It must be mentioned that the proposed active contour model is capable of only deflating the contour towards a desired object. Therefore the initial contour should be placed outside the target object. The main objective of this research is to capture sharp corners and discontinuous boundaries and as such, if the initial contour is placed inside the object, it makes it difficult to capture such protruding regions while the model is inflating. As a result, the balloon force cannot be introduced to the proposed model at this stage.

6 Conclusion

The complexity of discontinuous boundaries in X-ray medical images makes the segmentation task very difficult. In this paper, a new snake model is proposed to capture discontinuous boundaries present in X-ray medical images accurately by incorporating a priori knowledge of discontinuous region into the segmentation process. The results obtained after applying the technique on several synthetic and X-ray medical images show the performance of the proposed model even with complex discontinuities. Further studies on improving the algorithm to achieve accurate results on other medical images containing a high amount of noise and low contrast need to be explored.

7 References

1 McInerney, T., Terzopoulos, D.: 'Deformable models in medical image analysis: a survey', *Med. Image Anal.*, 1996, **1**, (2), pp. 91–108
2 Singh, A., Terzopoulos, D., Goldgof, D.B.: 'Deformable models in medical image analysis' (IEEE Computer Society Press, 1998, 1st edn.)
3 Hegadi, R., Kop, A., Hangarge, Hangarge, M.: 'A survey on deformable model and its applications to medical imaging', *Int. J. Comput. Appl., Spec. Issue Recent Trends Image Process. Pattern Recognit.*, 2010, **2**, pp. 64–75
4 Ma, Z., Tavares, J.M.R.S., Jorge, R.M.N.J.: 'A review on the current segmentation algorithms for medical images'. Proc. Int. Conf. on Imaging Theory and Applications (IMAGAPP), Lisboa, Portugal, February 2009, pp. 135–140
5 Kass, M., Witkin, A., Terzopoulos, D.: 'Snakes: active contour models', *Int. J. Comput. Vis.*, 1988, **1**, (4), pp. 321–331
6 Choi, W.P., Lam, K.-M., Siu, W.-C.: 'An adaptive active contour model for highly irregular boundaries', *Pattern Recognit.*, 2001, **34**, (2), pp. 323–331
7 McInerney, T., Terzopoulos, D.: 'T-snakes: topology adaptive snakes', *Med. Image Anal.*, 2000, **4**, (2), pp. 73–91
8 Cohen, L.D.: 'On active contour models and balloons', *CVGIP: Image Underst.*, 1991, **53**, (2), pp. 211–218
9 Lam, K.M., Yan, H.: 'Fast greedy algorithm for active contours', *Electron. Lett.*, 1994, **30**, (1), pp. 21–23
10 Xu, C., Prince, J.L.: 'Gradient vector flow: a new external force for snakes, computer vision and pattern recognition'. Proc. IEEE Int. Conf. on Computer Vision and Pattern Recognition, San Juan, USA, June 1997, pp. 66–71
11 Caselles, V., Kimmel, R., Sapiro, G.: 'Geodesic active contours', *Int. J. Comput. Vis.*, 1997, **22**, (1), pp. 61–79
12 Menet, S., Saint-Marc, P., Medioni, G.: 'B-snakes: implementation and application to stereo', *IEEE Trans. Image Process.*, 1990, **9**, (9), pp. 720–726
13 Meegama, R.G.N., Rajapakse, J.C.: 'NURBS snakes', *Image Vis. Comput.*, 2003, **21**, (6), pp. 551–562
14 Duncan, J.S., Ayache, N.: 'Medical image analysis: progress over two decades and the challenges ahead', *IEEE Trans. Pattern Anal. Mach. Intell.*, 2000, **22**, (1), pp. 85–106
15 Harris, C., Stephens, M.: 'A combined corner and edge detector'. Proc. Alvey vision conference, Manchester, UK, 1988, pp. 147–151
16 Ronfard, R.M.: 'Region-based strategies for active contour models', *Int. J. Comput. Vis.*, 1994, **13**, (2), pp. 229–251
17 Poon, C.S., Braun, M.: 'Image segmentation by a deformable contour model incorporating region analysis', *Phys. Med. Biol.*, 1997, **42**, (9), pp. 1833–1841
18 Cohen, L.D., Cohen, I.: 'Finite-element methods for active contour models and balloons for 2-D and 3-D images', *IEEE Trans. Pattern Anal. Mach. Intell.*, 1993, **15**, (11), pp. 1131–1147
19 Danielsson, P.E.: 'Euclidean distance mapping', *Comput. Graph. Image Process.*, 1980, **14**, (3), pp. 227–248
20 Xu, C., Prince, J.L.: 'Snakes, shapes, and gradient vector flow', *IEEE Trans. Image Process.*, 1998, **7**, (3), pp. 359–369
21 Malladi, R., Sethian, J.A., Vemuri, B.C.: 'Shape modeling with front propagation: a level set approach', *IEEE Trans. Pattern Anal. Mach. Intell.*, 1995, **17**, (2), pp. 158–175
22 Sapiro, G., Tannenbaum, A.: 'Affine invariant scale-space', *Int. J. Comput. Vis.*, 1993, **11**, (1), pp. 25–44
23 Kimia, B.B., Tannenbaum, A.R., Zucker, S.W.: 'Shapes, shocks, and deformations I: the components of two-dimensional shape and the reaction-diffusion space', *Int. J. Comput. Vis.*, 1995, **15**, (3), pp. 189–224
24 Sethian, J.A.: 'Level set methods and fast marching methods: evolving interfaces in computational geometry, fluid mechanics, computer vision, and materials science' (Cambridge University Press, 1999, 2nd edn)
25 Brigger, P., Unser, M.A.: 'Multiscale B-spline snakes for general contour detection'. Proc. Conf. Wavelet Applications in Signal and Image Processing VI, San Diego, CA, October 1998, pp. 92–102
26 Brigger, P., Hoeg, J., Unser, M.: 'B-spline snakes: a flexible tool for parametric contour detection', *IEEE Trans. Image Process.*, 2000, **9**, (9), pp. 1484–1496
27 Qin, H., Terzopoulos, D.: 'D-NURBS: a physics-based framework for geometric design', *IEEE Trans. Vis. Comput. Graph.*, 1996, **2**, (1), pp. 85–96
28 Staib, L.H., Duncan, J.S.: 'Model-based deformable surface finding for medical images', *IEEE Trans. Med. Imaging*, 1996, **15**, (5), pp. 720–731

doi: 10.1049/iet-ipr.2014.0106